Research Square

Preprints are preliminary reports that have not undergone peer review.
They should not be considered conclusive, used to inform clinical practice,
or referenced by the media as validated information.

An Online Monitoring Method for Measuring Ice Thickness of Transmission Lines Based on a Rotating Ring Electrode Array

Chao Gao
State Grid Henan Electric Power Company (China)
Zehui Liu
1515021282@qq.com

State Grid Henan Electric Power Company (China)
Zhongbing Lv
State Grid Henan Electric Power Company (China)
Wei Yang
State Grid Henan Electric Power Company (China)
Chuan Wu
State Grid Henan Electric Power Company (China)

Article

Keywords:

Posted Date: October 27th, 2026

DOI: https://doi.org/10.21203/rs.3.rs-11320121/v1

License: This work is licensed under a Creative Commons Attribution 4.0 International License.
Read Full License

Additional Declarations: No competing interests reported.

An Online Monitoring Method for Measuring Ice Thickness of Transmission Lines Based on a Rotating Ring Electrode Array

Chao Gao[1], Zehui Liu[1*], Zhongbin Lv[1], Wei Yang[1], Chuan Wu[1]

[1*]Electric Power Research Institute of State Grid Henan Electric Power Company, China.

*Corresponding author(s). E-mail(s): 1515021282@qq.com;

Abstract

Ice accretion on overhead transmission lines increases mechanical and electrical risks, while de-icing decisions require accurate ice-thickness data at the early growth stage. Capacitive sensing is compact and low power, but irregular natural accretion distorts the capacitance–thickness relation and most sensors have been validated only in climate chambers. Here we develop an online monitoring method based on a rotating ring electrode array. Four ring-shaped three-electrode units rotate on a motor-driven insulating shaft, allowing natural accretion to form a more uniform cylindrical ice layer. Three-dimensional electrostatic finite-element analysis optimized electrode geometry using signal strength, sensitivity, and penetration depth. A device integrating a 28-bit capacitance-to-digital converter, temperature–humidity sensing, and GPRS/LoRa transmission was tested under natural glaze and mixed-rime icing. Capacitance increased monotonically with thickness and saturated near a penetration depth of 12 mm. Maximum sensitivity reached 6.1 pF/mm, and mean deviations from computed capacitance were 2.37–4.83%. The results demonstrate the feasibility of rotating ring electrodes for online ice-thickness monitoring in natural icing environments and provide measurements for de-icing decisions.

Keywords: Transmission line icing, ice thickness, online monitoring, capacitive sensor, ring electrode array, natural icing

1 Introduction

Atmospheric icing increases conductor and tower loads, promotes galloping and unequal-tension faults, degrades insulation, and can cause outages [1–3]. De-icing must therefore be triggered from continuous, quantitative information on ice thickness during the early growth stage.

Existing monitors infer icing from span load or insulator-string tension, image features, or meteorological models. Mechanical methods measure integrated load rather than local thickness and require instrumented structures; optical methods degrade in fog, precipitation, darkness, and lens icing; meteorological models require site calibration [4–7]. Capacitive sensing is compact and low power because ice, water, and air have different permittivities [8–11].

Field deployment is limited by accretion shape and insufficient natural-icing validation. Under unilateral wind, a deposit becomes elliptical or wing-shaped; in our chamber tests, a 15 mm wing-shaped glaze deposit produced 36.22% less capacitance than an equal cylindrical deposit, whereas conductivity and ice-type effects were at most 7.46% and 20.63%, respectively. A fixed electrode therefore cannot transfer a chamber calibration curve reliably to the field.

This study proposes a rotating ring electrode array that converts irregular accretion into a more uniform cylindrical shell. Three-dimensional electrostatic finite-element analysis (FEA) is used to select the electrode geometry, a wireless monitoring device is implemented, and natural glaze and mixed-rime tests validate the method. The contribution is a physically shape-stabilized capacitive sensor with a quantified design procedure and field error analysis.

2 Measurement Principle and Sensor Configuration

2.1 Dielectric behavior and excitation frequency

Ice is a polar dielectric with Debye-type relaxation [13, 14]. Above roughly 100 kHz, its relative permittivity approaches 3.2 and dielectric loss is small, reducing sensitivity to water conductivity and temperature. Chamber tests on LGJ-500/35 conductor samples used water conductivities of 200–1120 μS/cm. At 10 mm equivalent thickness, the capacitance increase from 200 to 320, 640, and 1120 μS/cm was 2.71%, 3.75%, and 7.46%. The data followed

$$C = kh^e, \tag{1}$$

where C is capacitance, h is equivalent thickness, and k, e are fitting parameters. The fitted exponent was 0.2857 for glaze, 0.2438 for mixed rime, and 0.2331 for hard rime.

2.2 Rotating electrode concept

Unilateral wind produces eccentric or wing-shaped accretion [4]. At equal 15 mm thickness, the chamber capacitance was 49.12 pF for a cylindrical deposit and 36.06 pF for a wing-shaped deposit. The array therefore rotates slowly on an insulating shaft so that all azimuthal positions receive droplets and the deposit approaches a cylindrical shell. This removes the dominant shape error at the sensing stage rather than correcting it after measurement.

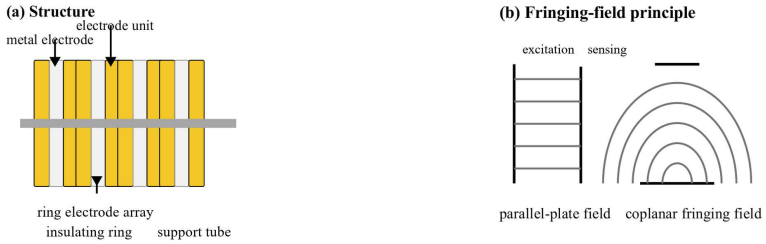


Fig. 1 Structure of the ring electrode array and fringing-field measurement principle.

2.3 Ring three-electrode array

Each unit contains two outer excitation rings and a middle sensing ring. Four units are mounted on a polytetrafluoroethylene (PTFE) support tube and wired in parallel. The fringing field between adjacent rings acts as a cylindrical parallel-plate capacitor; replacing air with ice of relative permittivity about 3.2 increases the measured capacitance (Figure 1).

3 Finite-Element Optimization and Device Implementation

3.1 Electrostatic model and indices

The non-uniform fringing field was analyzed with three-dimensional electrostatic FEA (COMSOL Multiphysics):

$$\nabla\cdot[\varepsilon_0\varepsilon_r(x,y,z)\nabla V(x,y,z)] = 0, \tag{2}$$

$$C = \frac{Q}{U} = \frac{1}{U}\oint_S \mathbf{D}\cdot \mathrm{d}\mathbf{S}. \tag{3}$$

The air domain was a 700 mm diameter, 1000 mm high cylinder; the ice shell varied from 0 to 20 mm in 1 mm steps with relative permittivity 3.2, PTFE was 2.55, and the copper electrodes were set to 1 V and 0 V. Signal strength, sensitivity $S = \Delta C/\Delta h$, and penetration depth (the thickness at which the increment reaches 95% of saturation) were used as performance indices.

3.2 Parameter selection

Six parameters were swept independently: coverage ratio f, electrode height H_e, thickness d_e, outer diameter D_e, unit number N, and spacing H_c (Figure 2). Increasing f raises signal and sensitivity but shortens penetration depth; $f = 2/3$ balances the indices. Increasing H_e extends penetration depth at the cost of signal, so $H_e = 8$ mm was selected. Electrode thickness has little field influence and $d_e = 2$ mm was selected. Larger D_e increases signal and sensitivity, motivating 24 and 36 mm prototypes. Signal scales nearly linearly with N and $N = 4$ limits sensor length; H_c has little influence

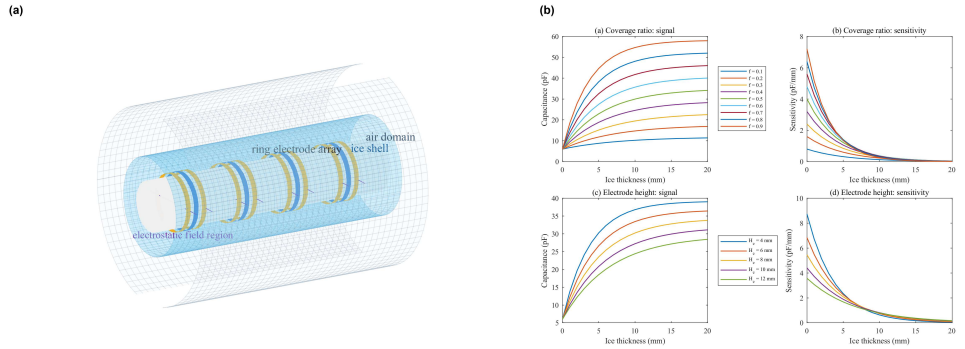


Fig. 2 Finite-element model and electrode-parameter optimization. (a) Three-dimensional electrostatic model of the ring electrode array. (b) Influence of electrode coverage ratio and electrode height on signal strength, sensitivity, and penetration depth.

Table 1 Structural parameters of the ring electrode array and relative error between measured and computed capacitance.

(a) Structural parameters

Parameter	Symbol	Value
Electrode height (mm)	H_e	8
Insulating ring height (mm)	H_i	6
Electrode thickness (mm)	d_e	2
Support tube thickness (mm)	d_s	2
Electrode outer diameter (mm)	D_e	24 / 36
Support tube outer diameter (mm)	D_s	20 / 32
Number of units	N	4
Unit spacing (mm)	H_c	18

(b) Relative error (%)

Ice type	D_e	Maximum	Minimum	Mean
Glaze	24	7.18	1.57	3.06
Glaze	36	5.75	1.97	2.37
Mixed rime	24	8.94	1.95	4.83
Mixed rime	36	6.85	1.03	2.58

and was set to 18 mm. The response saturated above about 12 mm. The selected structural parameters and the measured–computed errors are summarized in Table 1.

3.3 Device implementation

Brass electrodes and PTFE insulating parts were machined into the selected array; shielded cables and a grounded copper foil reduced parasitic coupling. A Texas Instruments FDC2214 capacitance-to-digital converter provided four-channel, 28-bit acquisition at a 10 MHz excitation frequency. An STM32F103RCT6 controller recorded capacitance, temperature, and humidity, while GPRS and LoRa links transmitted data. Measurements were sampled every 10 s and averaged over 60 s intervals. The fabricated array and host interface are shown in Figure 3.

4 Natural Icing Field Test

4.1 Test arrangement

Natural icing tests were conducted at a field observation site representative of severe icing environments. Sensors were mounted on a horizontal frame 1 m above ground, spaced 1 m apart, and protected by an IP67 enclosure. Wind speed ranged from 0.5 to 11.5 m/s with gusts up to 15 m/s. The device recorded capacitance, temperature,

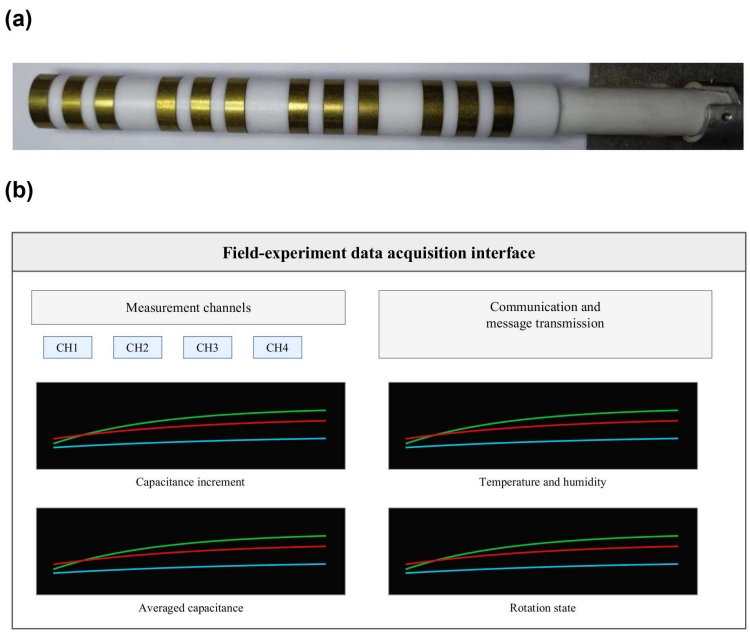


Fig. 3 Device implementation. (a) Fabricated rotating ring electrode array. (b) Host interface for online data acquisition.

and humidity automatically. Ice thickness was measured with a 0–150 mm vernier caliper (accuracy ±0.02 mm); three diameter readings were taken at each of three array sections and converted to thickness by

$$h = \frac{1}{2}\left[\frac{\sum_{i=1}^{n}\left(D_a(i) + D_b(i) + D_c(i)\right)}{3n} - D_e\right], \tag{4}$$

where $n = 3$. Caliper-perturbed capacitance samples were discarded, and the immediately preceding value was paired with each thickness measurement. Each cycle lasted 8–24 h; the shell was then melted, the array dried, and the next cycle started. Pairs were extracted at 1 mm thickness increments.

5 Results and Discussion

5.1 Natural-icing response

Glaze formed a smooth cylindrical shell, whereas mixed rime was opaque and porous (Figure 4). For glaze, the bare capacitances were 13.9 and 21.6 pF for $D_e = 24$ and 36 mm, increasing to 31.3 and 46.4 pF at 20 mm. Penetration depths were 11.6 and 12.1 mm, and peak sensitivities were 4.9 and 6.1 pF/mm. For mixed rime, the 20 mm capacitances were 27.6 and 42.7 pF and penetration depths were 12.6 and 12.5 mm (Figure 5). Its peak sensitivities, 2.6 and 4.1 pF/mm, occurred at 3 mm because the porous deposit initially covered the electrode incompletely.



Fig. 4 Natural ice deposits on the rotating ring electrode arrays: (a) glaze and (b) mixed rime.

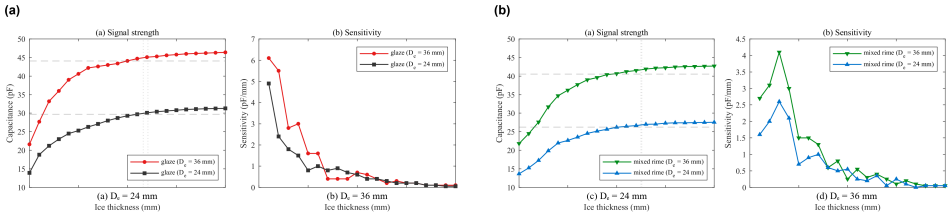


Fig. 5 Capacitance and sensitivity versus ice thickness under natural icing. (a) Glaze icing. (b) Mixed-rime icing.

5.2 Simulation–experiment comparison

Measured and computed curves had the same monotonic, saturating shape and diameter dependence (Figure 6). Mean errors were 3.06% and 2.37% for glaze on the 24 and 36 mm sensors, and 4.83% and 2.58% for mixed rime. Errors were largest at small thickness and for the porous mixed-rime shell. The main causes are the difference between electrostatic modeling and 10 MHz measurement, parasitic capacitance from adhesive and water films, natural fluctuations in wind and ice density, and incomplete shell coverage at early growth.

5.3 Ice type and engineering applicability

At equal thickness, glaze produced a larger capacitance than mixed rime, while penetration depth remained near 12 mm. The response amplitude and fitted power-law exponent therefore provide an auxiliary ice-type indicator; quantitative inversion is left for future work. The validated operating band is approximately 0–12 mm, with sensitivity up to 6.1 pF/mm and mean deviation below 4.83%. The sensor is suited to triggering and supervising de-icing during early accumulation, not to tracking growth beyond penetration depth. Larger electrode height can extend the range, while larger diameter increases signal and sensitivity.

Limitations are saturation beyond 12 mm, upward bias during wet growth, pointwise rather than span-wide measurement, and the need for longer unattended tests of the drive mechanism under freezing rain.

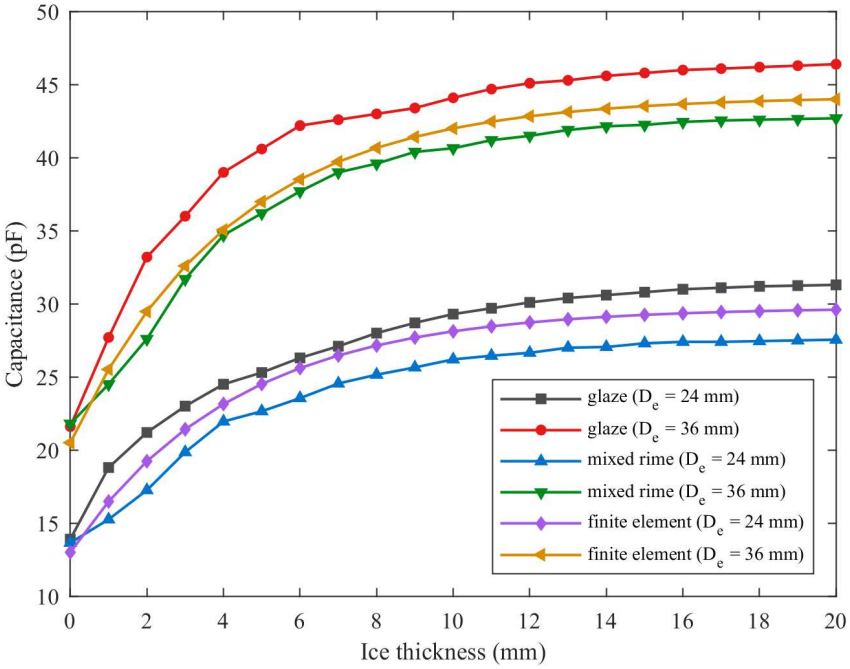


Fig. 6 Measured and computed capacitance versus ice thickness for both ice types and electrode diameters.

6 Conclusion

A rotating ring electrode array was developed and validated under natural glaze and mixed-rime icing. The main conclusions are:

1. Rotation converts irregular accretion into a near-cylindrical shell and removes the dominant shape error; a 15 mm wing-shaped deposit differed from a cylindrical deposit by 36.22% in capacitance.
2. FEA identified the sensitivity–penetration trade-off and selected $f = 2/3$, $H_e = 8$ mm, $d_e = 2$ mm, $N = 4$, $H_c = 18$ mm, and $D_e = 24/36$ mm, giving a penetration depth of about 12 mm.
3. Natural-icing tests produced maximum sensitivity of 6.1 pF/mm, penetration depths of 11.6–12.6 mm, and mean simulation–experiment deviations of 2.37–4.83%. Ice type affected response amplitude more than measuring range.

Future work will address wet-growth correction, joint inversion of ice type and thickness, range extension, and integration with load-current-transfer de-icing control.

Declarations

Funding

This work was supported by the Science and Technology Project "Research on Load Current Cyclic Transfer De-icing Technology for Bundle Conductors of 500 kV Transmission Lines" (Project No.: **52170225000J**).

Competing interests

The authors declare no competing interests.

Data availability

The field-test data supporting the findings of this study are available from the corresponding author on reasonable request.

Ethics declarations

Not applicable. The study did not involve human participants, human materials, live vertebrates, or higher invertebrates.

Author contributions

All authors contributed to the conception and design of the study, the investigation, interpretation of results, and revision of the manuscript. The corresponding author coordinated the project and manuscript submission.

AI use disclosure

A large language model was used for language editing and formatting; the authors remain responsible for the content and conclusions.

References

[1] M. Farzaneh, Ed., *Atmospheric Icing of Power Networks*. Dordrecht, The Netherlands: Springer, 2008, doi: 10.1007/978-1-4020-8531-4.

[2] J. Hu, L. Liu, X. Zhang, and Y. Ju, "A review of transmission line icing disasters: mechanisms, detection, and prevention," *Buildings*, vol. 15, no. 20, Art. no. 3757, 2025, doi: 10.3390/buildings15203757.

[3] J. Pohlman and P. Landers, "Present state-of-the-art of transmission line icing," *IEEE Trans. Power App. Syst.*, vol. PAS-101, no. 8, pp. 2443–2450, 1982, doi: 10.1109/TPAS.1982.317605.

[4] L. Makkonen, "Models for the growth of rime, glaze, icicles and wet snow on structures," *Philos. Trans. R. Soc. A*, vol. 358, no. 1776, pp. 2913–2939, 2000, doi: 10.1098/rsta.2000.0690.

[5] K. Ji, X. Rui, L. Li, A. Leblond, and G. McClure, "A novel ice-shedding model for overhead power line conductors with the consideration of adhesive/cohesive forces," *Comput. Struct.*, vol. 157, pp. 153–164, 2015, doi: 10.1016/j.compstruc.2015.05.014.

[6] Y. Hao, L. Huang, J. Wei, W. Liang, R. Pan, and L. Yang, "The detecting system and method of quasi-distributed fiber Bragg grating for overhead transmission line conductor ice and composite insulator icing load," *IEEE Trans. Power Del.*, vol. 38, no. 3, pp. 1799–1809, 2023, doi: 10.1109/TPWRD.2022.3222774.

[7] M. Hu, J. He, and M. Alsabaan, "Image identification method of ice thickness on transmission line based on visual sensing," *Mobile Netw. Appl.*, vol. 28, no. 5, pp. 1783–1792, 2023, doi: 10.1007/s11036-023-02244-1.

[8] M. C. Homola, P. J. Nicklasson, and P. A. Sundsbo, "Ice sensors for wind turbines," *Cold Reg. Sci. Technol.*, vol. 46, no. 2, pp. 125–131, 2006, doi: 10.1016/j.coldregions.2006.06.005.

[9] X. Zhi, H. Cho, B. Wang, C. Ahn, H. Moon, and J. Go, "Development of a capacitive ice sensor to measure ice growth in real time," *Sensors*, vol. 15, no. 3, pp. 6688–6698, 2015, doi: 10.3390/s150306688.

[10] Y. Zhu, X. Huang, Y. Tian, C. Ji, W. Cao, and L. Zhao, "Experimental study on the icing dielectric constant for the capacitive icing sensor," *Sensors*, vol. 18, no. 10, Art. no. 3325, 2018, doi: 10.3390/s18103325.

[11] W. Stocksreiter and H. Zangl, "Compact multifunctional wireless capacitive sensor system and its application in icing detection," *Sensors*, vol. 19, no. 24, Art. no. 5562, 2019, doi: 10.3390/s19245562.

[12] H. Ur Rahman, A. N. Malik, and I. Lazoglu, "Ice growth detection and the deicing using dual functional capacitive sensor," *Measurement*, vol. 237, Art. no. 115208, 2024, doi: 10.1016/j.measurement.2024.115208.

[13] V. F. Petrenko and R. W. Whitworth, *Physics of Ice*. Oxford, U.K.: Oxford University Press, 1999.

[14] N. Bjerrum, "Structure and properties of ice," *Science*, vol. 115, no. 2989, pp. 385–390, 1952, doi: 10.1126/science.115.2989.385.

[15] F. Xu, D. Li, P. Gao, W. Zang, Z. Duan, and J. Ou, "Numerical simulation of two-dimensional transmission line icing and analysis of factors that influence icing," *J. Fluids Struct.*, vol. 118, Art. no. 103858, 2023, doi: 10.1016/j.jfluidstructs.2023.103858.

[16] Z. Wang, "Recent progress on ultrasonic de-icing technique used for wind power generation, high-voltage transmission line and aircraft," *Energy Build.*, vol. 140, pp. 42–49, 2017, doi: 10.1016/j.enbuild.2017.01.072.